# Multicolor two-photon light-patterning microscope exploiting the spatio-temporal properties of a fiber bundle

Antonio Lorca-Cámara, Christophe Tourain, Vincent de Sars, Valentina Emiliani, Nicolò Accanto

Research Article | Vol. 15, No. 4 / 1 Apr 2024 / Biomedical Optics Express 2094
Biomedical Optics EXPRESS

# Multicolor two-photon light-patterning microscope exploiting the spatio-temporal properties of a fiber bundle

ANTONIO LORCA-CÁMARA,[1] CHRISTOPHE TOURAIN,[1] VINCENT DE SARS,[1] VALENTINA EMILIANI,[1,2] AND NICOLÒ ACCANTO[1,*]

[1]Sorbonne Université, INSERM, CNRS, Institut de la Vision, 75012 Paris, France
[2]valentina.emiliani@inserm.fr
[*]nicolo.accanto@inserm.fr

**Abstract:** The development of efficient genetically encoded indicators and actuators has opened up the possibility of reading and manipulating neuronal activity in living tissues with light. To achieve precise and reconfigurable targeting of large numbers of neurons with single-cell resolution within arbitrary volumes, different groups have recently developed all-optical strategies based on two-photon excitation and spatio-temporal shaping of ultrashort laser pulses. However, such techniques are often complex to set up and typically operate at a single wavelength only. To address these issues, we have developed a novel optical approach that uses a fiber bundle and a spatial light modulator to achieve simple and dual-color two-photon light patterning in three dimensions. By leveraging the core-to-core temporal delay and the wavelength-independent divergence characteristics of fiber bundles, we have demonstrated the capacity to generate high-resolution excitation spots in a 3D region with two distinct laser wavelengths simultaneously, offering a suitable and simple alternative for precise multicolor cell targeting.



## 1. Introduction

In recent years, the field of neuroscience has been revolutionized by optogenetics, which enables to induce or inhibit neuronal activity in specific populations of neurons by using light [1–4]. To gain a deeper understanding of how spatial and temporal patterns of neuronal activity in the brain influence perception and behavior, advanced optical techniques are required to control the activity of groups of neurons with single-cell resolution and in a reconfigurable manner. In pursuit of this goal, researchers have developed optical systems that combine two-photon excitation (2PE) [5,6], which increases optical sectioning and penetration depth through scattering media, with computer-generated holography (CGH) [7] or generalized phase contrast (GPC) [8] utilizing spatial light modulators (SLMs) to precisely and dynamically target single or groups of neurons in large volumes [9,10]. Pioneering experiments using similar methods have started to show that precise optogenetics photostimulation of selected neurons in the mouse brain can influence animal behavior and affect perception [11–14] or influence neuronal population dynamics [15]. Sequential optogenetic activation of one or few cells at cellular resolution also enabled *in vitro* and *in vivo* high throughput connectivity mapping [16–19].

In general, to efficiently photostimulate groups of neurons with 2PE, a SLM is used to multiplex the excitation onto different targets, in combination with spiral scanning [20] or to generate large excitation spots [21] to cover the whole soma of a neuron. In the latter case, to overcome the loss of axial resolution that a laterally extended excitation spot would cause, lateral light shaping is combined with the temporal focusing (TF [22–24]) technique. TF is based on a diffraction grating that decomposes the spectral wavelengths of an ultrashort laser pulse, thus increasing the pulse duration and preventing 2PE until all the colors are recombined at the sample plane [22,23]. Most implementations that combine CGH or GPC and TF can only achieve 2P photostimulation with

#507690 https://doi.org/10.1364/BOE.507690
Journal © 2024 Received 11 Oct 2023; revised 9 Dec 2023; accepted 2 Jan 2024; published 4 Mar 2024

Biomedical Optics EXPRESS

cellular resolution and high temporal precision within a 2D region [25,26], which corresponds to the image plane of the diffraction grating. To extend experiments to a 3D volume, additional optical elements are generally required beyond the diffraction grating and a single SLM. For instance, a second SLM to displace laterally and axially the temporally focused shape generated by the first SLM (or a fixed phase mask) on the TF grating [27–29]. Alternative approaches for the generation of 3D temporally focused patterns used a large Gaussian beam [30] and, in its revised form, a rotating diffuser between the diffraction grating and the multiplexing SLM [31], or a galvanometric mirror, placed before the SLM, to sequentially scan vertically aligned holograms for ultrafast sequential light targeting [32].

Besides the use for optogenetics, temporal focused multitarget illumination has been also used for multitarget functional imaging using genetically encoded calcium [33,34] or voltage indicators [35], or for fast scanning volumetric calcium imaging with temporally focused spots [36].

One of the significant challenges arising from the use of the diffraction grating for TF occurs when attempting to tune the incident wavelength or coupling multiple colors, which is important in experiments that require, for instance, dual-color scanless imaging and photostimulation [34,37,38], bidirectional control of neuronal activity through dual-color activation and inhibition of the same or different cells [37,39,40] or single color scanless (or TF scanned) illumination [33,36].

Because TF is based on the spatial dispersion of the different wavelengths of the laser beam at different angles [23], lasers beams with different central wavelengths would be diffracted at different angles. This requires to readjust the angle between the incident or the reflected beam and the grating to maintain a constant deflection for the different wavelengths. Although dual-color 2PE with TF was used to image specimens labeled with different fluorophores [41,42], the experimental system needed a switching element (such as galvanometric mirrors) to compensate for the different grating angles, increasing the system's complexity. Moreover, this compensation is limited to a narrow range of excitation wavelengths.

In this study, we present a novel optical configuration for the generation of single and multicolor 2D and 3D light patterns, where the diffraction grating for TF is replaced by a multi-core optical fiber bundle. This system capitalizes on the core-to-core delay dispersion inherent to the fiber bundle, a concept previously detailed in Ref [43], allowing us to maintain micrometer-level axial resolution independently of the spot size. Our results demonstrate that this approach simplifies the optical setup, obviating the necessity of two SLMs for 3D light patterning, or of a rotating diffuser. Furthermore, we demonstrate that substituting the diffraction grating with a fiber bundle preserves the propagation angle after exiting the fiber bundle, irrespective of the excitation wavelength. Consequently, this innovation enables the generation of 2D and 3D multicolor light patterns using a single beam path.

## 2. Materials and methods

### 2.1. Optical setup

The optical setup (Fig. 1(a)) uses two different laser sources: 1) a low repetition rate laser (Goji, Amplitude, central wavelength of 1030 nm, pulse duration of 150 fs, total power of 4 W, repetition rate of 10 MHz) and 2) a high repetition rate laser (Spark Alcor, central wavelength of 920 nm, pulse duration of 120 fs, total power of 4 W, repetition rate of 80 MHz) whose output powers are controlled by a lambda-half waveplate and a polarizer. The beam coming from each laser, after being combined with a dichroic mirror, is focalized with a short focal length lens (f0 = 18 mm) in the same region of the fiber bundle (Fujikura model FIGH-15-600N, inter-core distance ~4.5 µm, length of 2 meters, diameter of 550 µm), illuminating the same number of cores. The spot size that illuminates the fiber bundle, and thus the spots size at the sample plane, are modified

Biomedical Optics EXPRESS

by moving the lens (f0) placed before the fiber bundle with a translational stage that adjusts the distance between f0 and the fiber bundle and thus the defocus (Fig. 1(b)).

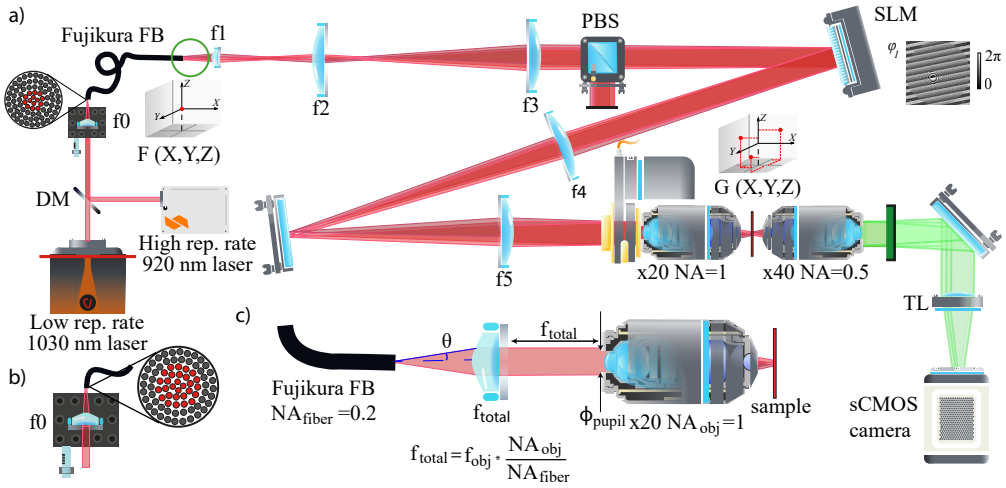


**Fig. 1. Experimental setup for a multicolour 3D light-patterning 2P microscope. a)** The Goji laser (4 W, 1030 nm, 10 MHz, 150 fs) and the Spark laser (4 W, 920 nm, 80 MHz, 120 fs), coupled with a dichroic mirror (DM), are focused (f0 = 18 mm) at the entrance of the fiber bundle (FB) illuminating multiple cores. After the fiber bundle (NA = 0.2) the light is collimated with a lens f1 = 8 mm (NA = 0.5). A telescope is used to match the beam with the SLM (f2 = 150 mm and f3 = 600 mm) and another telescope to match the size of the objective pupil (x20 NA = 1) with lenses (f4 = 200 mm and f5 = 300 mm). The total magnification of the system is x5.3, which maximizes the number of cores (around 300 cores for a 15 µm diameter spot) thus minimizing the power per core for a given total power. A polarized beam splitter (PBS) ensures that the correct polarization is sent to the SLM and rejects half of the light coming from the fiber bundle. The excitation objective can be moved axially with a piezoelectric motor to measure the axial profiles of the spots in the sample plane. The 2P fluorescence is measured using an inverted objective (x40 NA = 0.5) and a lens (TL = 180 mm) with an sCMOS camera. b) Input side of the fiber bundle illumination, showing that by moving the f0 lens - fiber bundle relative position, we can defocus the light to change the number of spots we illuminate, thus changing the spot size in the sample plane. c) Simplified optical scheme of the system where all the lenses between the fiber bundle and the excitation objective are reduced to an equivalent lens of focal $f_{total}$, which is determined by the excitation objective we use, considering a complete illumination of the objective back aperture, and the $NA_{fiber}$.

To compensate for the dispersion of the fiber bundle and additional optical elements, we adjust the pulse compressors inside the lasers with an internal dispersion control (around -90000 $fs^2$) [43]. At the fiber bundle output, the beam is collimated with an aspheric lens of NA = 0.5 (f1 = 8 mm, A240-B, Thorlabs). After that, a telescope magnifies the laser beams by a factor of 4 (f2 = 150 mm and f3 = 600 mm) to fill the screen of the SLM (LCOS-SLM X13138-03, Hamamatsu Photonics, resolution 1272 × 1024 pixels, 12.5 µm pixel size). The SLM is illuminated with an angle of 10 degrees to ensure proper performance. We experimentally verified that, with the beam divergence at the fiber bundle output and the lenses used, the beam at the SLM had a diameter, D, of 12.5 mm, matching the short side of the SLM screen. This value enables deriving the NA of the fiber bundle as $NA_{fiber} = \frac{D/2}{f_{eq}} = \frac{12.5/2}{32} = 0.2$, where $f_{eq} = \frac{f_1 \cdot f_3}{f_2}$, represents the equivalent focal lens of the lenses placed between the fiber bundle and the SLM. A second telescope (f4 = 200 mm and f5 = 300 mm) conjugates the SLM plane with the entrance of the microscope objective

Biomedical Optics EXPRESS

(Olympus XLUMPlanFL N 18/12 20XW, NA =1), filling its back aperture. Because the fiber bundle randomizes the input polarization, a polarizing beam splitter is placed before the SLM to select only the horizontal components (half of the total input light) and minimize the intensity of the zero (non-diffracted) order after the SLM. The SLM, placed at the Fourier plane of the fiber bundle output, multiplexes the original spot, which is composed of multiple illuminated fiber bundle cores, to generate 2D and 3D light patterns at the sample plane. The maximal reachable 2D FOV ($\Delta x_{max} \times \Delta y_{max}$) depends on the effective objective NA and the number of pixels of the SLM [44]: $\Delta x_{max} \times \Delta y_{max} = \frac{\lambda \cdot N}{4 \cdot NA_{obj}} \times \frac{\lambda \cdot N}{4 \cdot NA_{obj}}$. The phase holograms displayed by the SLM are calculated using a Gerchberg-Saxton algorithm [45]. Because the SLM is a diffractive optical element, the generated deflection angles depend on the laser wavelength. Different phase masks are therefore calculated for each laser wavelength and displayed on the SLM at different times. A beam blocker is placed in the plane between f4 and f5 to block the 0th order of the SLM. A custom-designed software, Wavefront-Designer V, written in C++ and using the open graphic library Qt 5.15.2, controls the SLM for the dynamic CGH configuration. The software also includes phase corrections for the first-order Zernike aberrations and the possibility to add a calibration mask to homogenize the fluorescence intensity distribution in the 3D field of view (FOV). The software also uses the capabilities of the Cuda GPU to accelerate processing speed, which were added to take advantage of both CPU and GPU capacity to calculate 3D patters even more efficiently [46,47].

The magnification of the system, from the fiber bundle output to the sample plane can be expressed as $\approx \frac{NA_{obj}}{NA_{fiber}}$, under the condition that the excitation beam completely fills the objective pupil ($\phi_{pupil}$). This expression can be derived by looking at the simplified schema of Fig. 1(c)) where the lenses ($f_{1-5}$) between the fiber bundle and the objective are replaced with a single lens of equivalent focal length $f_{total} = \frac{f_1 \cdot f_3 \cdot f_5}{f_2 \cdot f_4}$, and considering the corresponding expressions for the fiber bundle and objective numerical apertures: $NA_{fiber} \approx tan(\theta) = \frac{\phi_{pupil}}{2 \cdot f_{total}}$ and $NA_{obj} \approx \frac{\phi_{pupil}}{2 \cdot f_{obj}}$. The total magnification (M) of the system can be then expressed as $M = \frac{f_{total}}{f_{obj}} \approx \frac{NA_{obj}}{NA_{fiber}}$. This, given that, in our system $NA_{obj} = 1$ and $NA_{fiber} = 0.2$, results in a total magnification of $\approx 5$ in agreement with the measured value of 5.3. As a result, the generation of e.g. a spot of ~15 µm of lateral size corresponds to a spot of 80 µm diameter at the fiber bundle input corresponding to the illumination of ~300 cores.

### 2.2. Detection system and axial resolution measurements

The patterns generated by the SLM and focused by the excitation objective illuminate a thin fluorescent film made of a spin coated layer of rhodamine-6 G in polymethyl methacrylate (2% w/v in chloroform), and the 2P-excited fluorescence is collected by a second objective (Nikon, PLAN 40X, 0.7 NA) in transmission geometry and detected by a sCMOS camera (Orca Flash 4.0 C11440, Hamamatsu) using a tube lens (TL = 180 mm) and 2 IR blocking filters (Thorlabs TF1) (Fig. 1(a)). For characterizing the axial resolution, a z-step piezoelectric scanner (PI N-725.2A PIFOC) is used to axially scan the excitation objective over the desired z range in steps of 2 µm to obtain 3D stacks of images, while the second objective is fixed and focused on the fluorescent film plate.

The sCMOS camera is controlled with MicroManager and synchronized with the z-stack piezoelectric scanner of the excitation objective to measure the axial profiles of the spots created in the fluorescent sample. The recorded stacks are analyzed using Matlab and ImageJ. The 2P fluorescence values for each spot are obtained by integrating the intensity of all the pixels of the camera in a circular area containing the spot. Axial intensity distributions are obtained by integrating the intensity of the pixels in the same area for each plane of the recorded stack. The axial confinement values are reported as the full-width at half maximum (FWHM) of the axial profiles of the spots fitted with a Lorentzian model. Statistical data in axial resolution measurements are

Biomedical Optics EXPRESS

reported as mean ± standard deviation, and as averaged normalized mean ± standard deviation for 2P fluorescence signal measurements.

## 3. Results

### 3.1. Axial resolution for extended spots with a fiber bundle

We first characterized the axial resolution of a single spot that encompasses ~ 300 cores of the fiber bundle and results in a disk of 15 µm in diameter at the sample plane, at the center of the FOV. As recently demonstrated, the inter-core delay dispersion of these fiber bundles, enables maintaining micrometer size axial resolution through a 2P fiberscope [43] independently of the laterally extension of the excitation spots. In practice, when multiple cores are illuminated simultaneously with an extended spot, the pulses from each core arrive at the sample plane at slightly different times due to small variations in the shape and size of the cores (Fig. 2(a)) [48]. This has the same consequence of TF, namely, a decrease of the out-of-focus 2PE, and maintains the axial confinement independent on the lateral spot size.

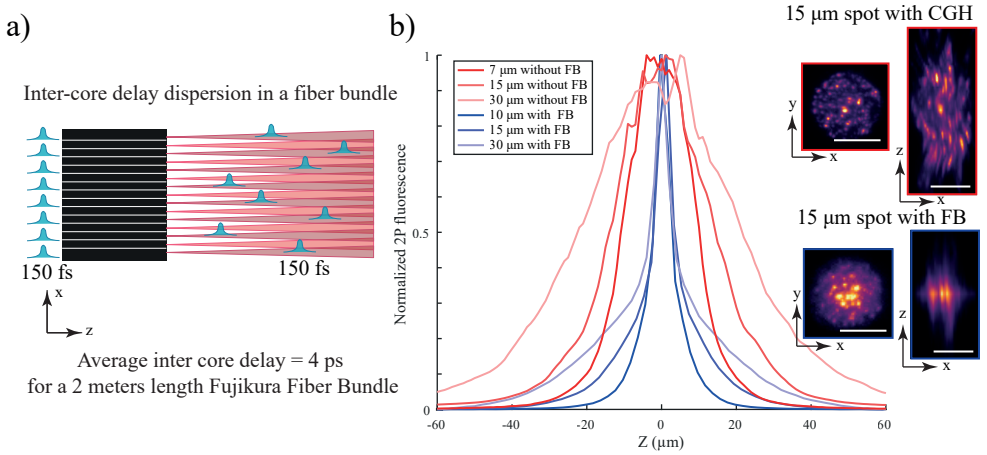


**Fig. 2. Characterization of the axial resolution for extended spots with and without the fiber bundle. a)** Schematic representation of the inter-core delays experienced by an ultrashort laser pulse ($\tau_0$ = 150 fs) when propagating through multiple cores of a ~2 m length Fujikura fiber bundle. b) Axial profiles of extended spots of 7, 15 and 30 µm created with fiber bundle (FB), corresponding to 65, 300 and 1200 illuminated cores, and with CGH without the fiber bundle. Insets: example of the front view (x,y) and the side view (x,z) of the 2P fluorescence signals generated by the 15 µm diameter spot with and without the fiber bundle. The axial confinement obtained with the fiber bundle is ~8 µm i.e. 2-4 times smaller than what achievable without the fiber bundle (~20-40 µm) by using 1 mW/core. Scale bar = 10 µm.

This effect is demonstrated in Fig. 2(b) where we compare the axial confinement of spots of different sizes generated at the center of the FOV by conventional CGH with spots that are propagated through the fiber bundle. As one can clearly see, the axial resolution of the spots is reduced to ~8 µm when using a fiber bundle and it shows little dependence on the lateral spot size compared to the axial resolution of CGH spots (axial resolution = 20 - 40 µm).

### 3.2. Effect of self-phase modulation on 2PE efficiency and axial resolution

In this section, we characterize the effect of the laser powers on the 2PE efficency and axial resolution. As descibed in the methods, in the current system, the spots at the sample plane are

Biomedical Optics EXPRESS

all replicas, generated by the SLM, of the same original spot created at the fiber bundle exit. To produce many excitation spots at the sample with sufficient power per spot, we therefore need to increase the total power at the fiber bundle entrance. As previously shown [49–52], one of the main challenges associated with using high laser powers through optical fibers or fiber bundles, is the occurrence of nonlinear effects as self-phase modulation (SPM), which can distort the laser pulses traveling through the fiber bundles, and correspondingly reduce the 2PE efficiency and axial resolution. For fibers similar to the one used in this study, the threshold for SPM when using an 80 MHz repetition rate laser at a wavelength of 850 nm is of ~10 mW/core [52], which corresponds to a pulse energy per core of 0.12 nJ.

To characterize the effects of SPM on the pulse broadening and axial resolution, for the lasers and wavelengths used in this study (920 nm and 1030 nm; 80 and 10 MHz repetition rate) we performed two separate sets of measurements. In a first set of experiments, we measured the 2P fluorescence generated by a 15 μm spot at constant power into the rhodamine sample, while increasing the power per core. This was achieved by adding a second power control at the output of the fiber bundle which maintains constant the power at the sample plane while a first power control increases the power per core sent to the entrance of the fiber bundle. The power per core was calculated by dividing the power measured at the output of the fiber bundle (which is ~ 60% of the power at the entrance of the fiber bundle) by the number of cores illuminated (~300 cores). Because the 2PE is inversely proportional to the laser pulse duration ($\tau$), measuring the fluorescence decrease as a function of the power per core ($P_{core}$), for a constant power into the sample, gives an indirect measurement of the effect of the SPM on the pulse broadening. Considering that the measurements of 2PE when low $P_{core}$ are used, i.e. $2PE_0$, correspond to the shortest pulse duration $\tau_0$, we can write the following equation: $\frac{2PE(\tau)}{2PE_0} = \frac{\tau_0}{\tau}$, where $\tau_0$ = 150 fs and $\tau_0$ = 120 fs (i.e. the nominal pulse duration from the laser manufacturers) for the low and high repetition rate laser, respectively. Using this equation, we obtained the values for $\tau$ reported in Fig. 3 for different laser powers. We found that at the maximum power used of 8 mW/core (corresponding to 0.1 and 0.8 nJ for the high and low repetition rate lasers, respectively), the laser pulse increased to 190 fs and 480 fs, for each laser (Fig. 3(a) and 3(b)) which corresponds to a 50% and 210% of pulse broadening ($\Delta\tau$) with respect to the initial laser pulse duration (see Supp. Figure 1 for pulse broadening dependence on the peak power for both lasers used). A linear relation $\tau(P_{core}) = \tau_0 + \Delta\tau(P_{core}) = \tau_0 + K \cdot P_{core}$ was found to well represent the experimental data in the range of powers used in the graphs. We therefore used such a relation to fit the data point by letting the parameters $\tau_0$ and K vary freely and obtained the curves plotted in Fig. 3(a) and 3(b).

Secondly, we measured the axial profile of a single 15 μm spot focused on a thin fluorescent layer of rhodamine in the center of the FOV (x = y = z = 0) using different powers per core for both lasers. As shown in (Fig. 3(c) and 3(d)), the FWHM of the axial profiles increases when illuminating the fiber bundle with higher powers per core. Specifically, the axial resolution changes from ~6 to ~7 μm for the high repetition rate laser and from ~5 to ~8 μm for the low repetition rate laser. This effect can be explained by the broadening of pulses due to SPM, discussed earlier. Specifically, with a constant inter-core delay dispersion (as it depends on a property of the fiber), the longer the pulses, the more likely pulses from different cores will overlap, resulting in an increased out-of-focus excitation and therefore loss of axial resolution.

### 3.3. Optical characterization of 2D and 3D pattern generation

In this section, we demonstrate the capability of the system for creating multiple 2PE spots, in a volume, using two wavelengths (920 nm and 1030 nm). To this end the two lasers are focalized to illuminate the same cores at the fiber bundle entrance, and the SLM, positioned after the fiber bundle, is used to multiplex and displace the replicas of the original spots by using for each wavelength the corresponding phase mask. To be noted that, to simulate experimental conditions

Biomedical Optics EXPRESS

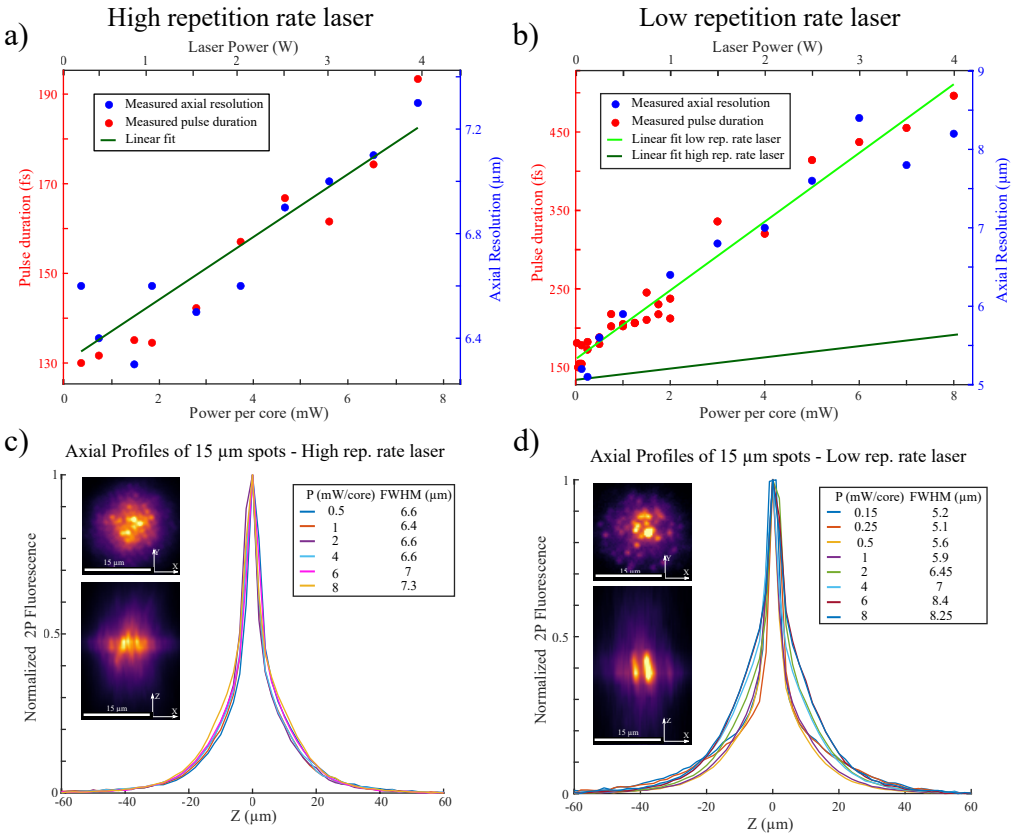


**Fig. 3. Optical characterization of a single spot through a fiber bundle. a, b)** In blue, measurements of the FWHM of the axial profiles in c, d) and in red, the calculated pulse duration of a 15 μm diameter spot in the sample plane for different powers, for the high and low repetition rate laser respectively. The pulse duration after the fiber bundle is obtained from the 2P fluorescence measured in the sample as described in the text. The laser pulse duration increases as the power density in the fiber bundle increases due to the SPM. The solid green line indicates a linear fit $\tau = K \cdot P_{core} + \tau_0$ between the power per core ($P_{core}$) and the pulse duration ($\tau$). From the fit we obtain K = 7.8 fs/mW and $\tau_0$ = 123 fs for the high repetition rate laser, and K = 43.8 fs/mW and $\tau_0$ = 160 fs for the low repetition rate laser, respectively. c, d) Measurements of the normalized axial profile of the 2P fluorescence of a 15 μm diameter spot in the sample plane at different powers, while illuminating ~300 cores in the fiber bundle with the 920 nm (c) and 1030 nm (d) laser. The power per core is determined by dividing the power measured at the fiber bundle output by the number of cores. Bottom right insets: front (x,y) and side (x,z) view of a 15 μm spot when using 2 mW/core.

Biomedical Optics EXPRESS

in which the setup is used to target the largest number of cells, in what follows, we always use the highest input laser power (4 W, ~8 mW/core). This leads to suboptimal pulse durations and axial resolutions, particularly for the low repetition rate laser.

We first demonstrate the possibility of creating a two-color distribution of 2PE spots on a single plane, on the largest 2D FOV allowed by the system (limited by the maximal angles the SLM can produce [44]). To homogenize the relative intensity of different spots at different distances from the center of the FOV, we applied for the two wavelengths the same diffraction efficiency correction mask on the SLM [27] (Fig. 4(a)).

As the SLM is a diffractive element, the deflection angles, and consequently, the x and y positions of the spots at the sample plane, depend on the incoming wavelength (Fig. 4(b)). This results in a wavelength-dependent calibration offset required to match the intended and effective positions of the spots. To compensate for this effect, when generating spatially overlapping spot distributions for the two wavelengths, we added a further relative scaling factor of 0.88 to the phase masks that control the spot generation with the laser at 1030 nm. This enables the creation of overlapping patterns at the sample plane, with the appropriate and sequentially applied phase mask for each wavelength, as shown in Fig. 4(b).

In Fig. 4(c) we show the obtained 2P fluorescence signal and the axial resolution of multiple spots generated from different patterns using the two lasers simultaneously (10 spots per pattern, 4 different patterns). We found values for the axial resolutions comprised between 8 and 18 µm, with a mean FWHM = 15 µm (standard deviation = 3 µm) at 920 nm and between 14 and 20 µm, with a mean FWHM = 16 µm (standard deviation = 2 µm) at 1030 nm.

Finally, we demonstrate the ability to create 3D two-color excitation patterns in a volume of $380 \times 380 \times 300$ µm$^3$ (Fig. 5). The average axial resolution (FWHM) of the spots is 20 µm at 920 nm and 24 µm at 1030 nm. There is a worsening of the axial resolution in both x-y plane and in z direction as we moved away from the center of the FOV, which we attribute to larger aberrations. The lateral profile for different spots in the volume for both lasers was also characterized to confirm that the properties of the spots were well-maintain throughout the entire FOV (Supp. Figure 2). Similar to what was done for 2D two-color generation of spots, a scaling factor (= 0.88) was added to the phase masks that control the 1030 nm beam.

With these results, we have demonstrated that our method can produce nearly uniform (std ~ 30%) two-color distributions of axially confined spots across a FOV of at least $380 \times 380 \times 300$ µm$^3$.

### 3.4. System capabilities

Here, we analyze the different parameters that need to be considered when designing an optical system tailored to diverse experimental conditions. This involves finding a balance between optimizing the available power (and consequently the achievable number of spots), and the achievable axial resolution and FOV. This is especially relevant for the current system, where increasing the number of spots at the sample plane requires increasing the power per core, $P_{core}$, at the fiber bundle, which, because of the SPM effect, can be detrimental for the 2PE efficiency and the axial resolution.

As explained in the methods, the condition on the optical magnification between the fiber output and the sample plane required to fill the pupil of the objective becomes $M \approx \frac{NA_{obj}}{NA_{fiber}} \sim 5$ when considering $NA_{fiber}$= 0.2 and an objective with $NA_{obj} = 1$. An excitation spot of diameter $\phi_{sample}$ at the sample plane corresponds to a diameter of $\phi_{fiber} = M \cdot \phi_{sample}$ at the fiber bundle. If we call the inter-core distance of the fiber bundle $\phi_{core}$, then the total number of cores illuminated by a spot can be expressed as $N_{cores} = \left(\frac{\phi_{fiber}}{\phi_{core}}\right)^2 = \left(M \cdot \frac{\phi_{sample}}{\phi_{core}}\right)^2 \approx \left(\frac{NA_{obj}}{NA_{fiber}} \cdot \frac{\phi_{sample}}{\phi_{core}}\right)^2$. For our experimental conditions $\phi_{core} = 4.5$ µm and considering a spot size at the sample of diameter $\phi_{sample} = 15$ µm, we obtain $N_{cores} \cong 300$ cores.

Biomedical Optics EXPRESS

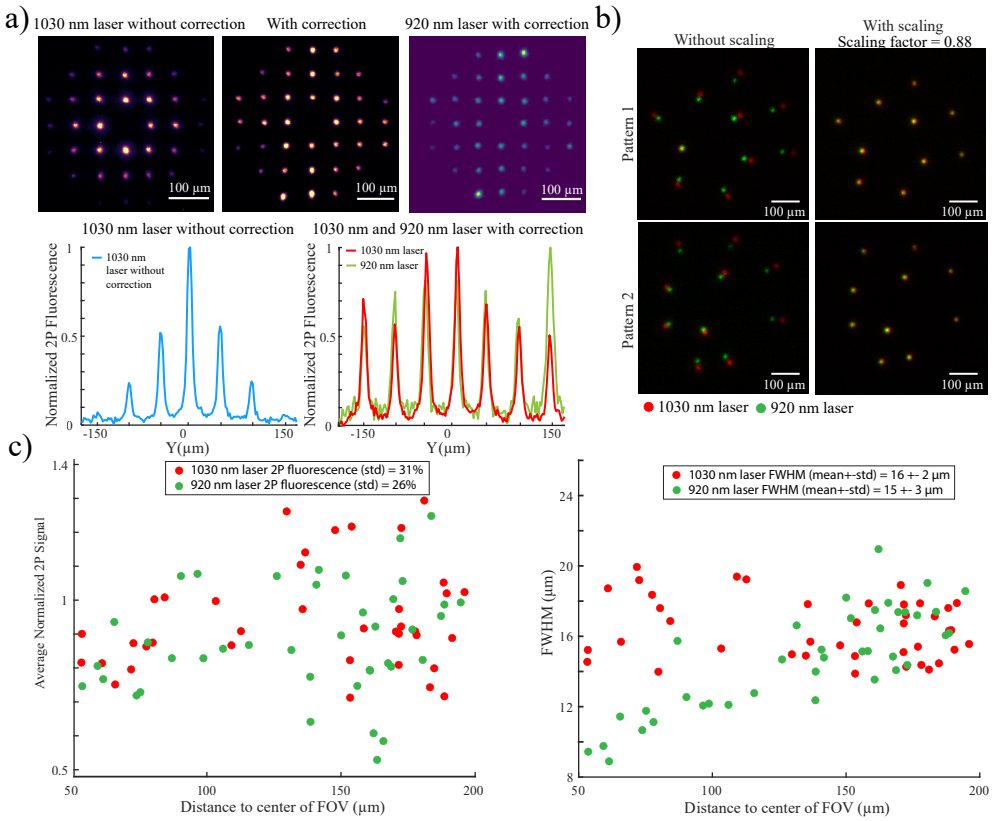


**Fig. 4. Optical characterization of multiple spots multiplexed in 2D with the SLM through a fiber bundle. a)** Top: Example of the recorded 2P fluorescence signal in the sample plane when a pattern (36 spots) without (left) and with (center and right) the correction is created for the two lasers in the 2D FOV. Bottom: Examples of the 2P fluorescence signal (a.u.) for a line of spots distributed along the Y axis. Left (blue): Diffraction efficiency correction is not applied so that a clear dependence of the 2P fluorescence with the distance to the center is shown. Right (red and green): diffraction efficiency correction is applied after a calibration to homogenize the 2P intensity distribution for both lasers. b) Example of 2P fluorescence signal in the sample plane when two patterns (10 spots per pattern) are created with the two different lasers. On the left, patterns 1 and 2 are applied to both lasers without applying the scaling factor. On the right, the scaling factor (= 0.88) is applied to the 1030 nm laser to produce overlapping spots. c) Left: Average normalized 2P signal of the spots randomly distributed in a 2D FOV of $380 \times 380$ µm$^2$ as a function of the distance to the center of the FOV for the two different lasers after the diffraction efficiency correction mask is applied. Right: FWHM of the axial profiles of the spots randomly distributed in a 2D FOV of $380 \times 380$ µm$^2$ as a function of the distance to the center of the FOV for the two different lasers.

Biomedical Optics EXPRESS

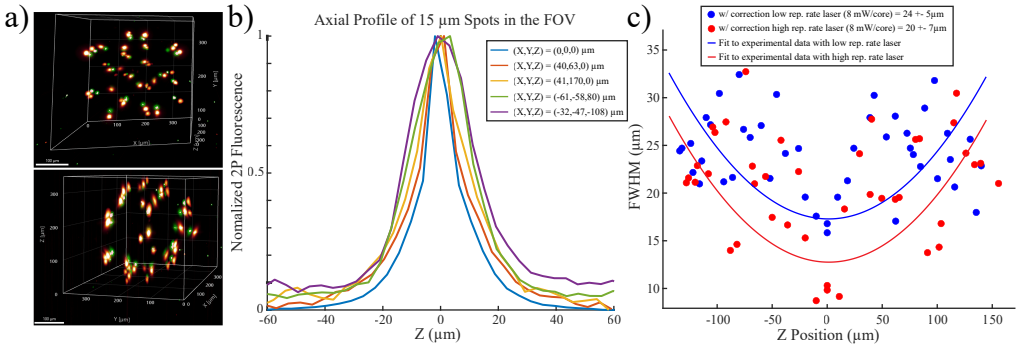


**Fig. 5. Optical characterization of multiple spots multiplexed in a 3D volume with the SLM through a fiber bundle. a)** Example of the recorded 2P fluorescence signal in the sample plane when 42 spots are created in a 3D FOV of $380 \times 380 \times 300$ µm$^3$ with both colors (green for the laser at 920 nm and red for the laser at 1030 nm) Top: (x,y) front view. Bottom: (y,z) side view. b) Axial profiles of some spots distributed in the 3D FOV at different (x, y, z) positions with the 1030 nm laser. c) FWHM of the axial profiles of the spots distributed in the 3D FOV in as a function of the axial position (z) for random (x, y) coordinates for two different wavelengths propagated through the fiber bundle (920 nm in red and 1030 nm in blue).

To calculate the total power at the sample plane and the 2PE efficiency, which depends on the pulse broadening, we first consider the power losses between the laser output and the sample plane within our experimental system. These losses are given by several components: the fiber bundle (transmission of 60%, $T_{\text{fiber}}$), the PBS (transmission of 50%), the SLM (reflection of the 1$^{\text{st}}$ diffraction order of 70%) and the excitation objective (transmission of 50-60% at the wavelengths used, $T_{\text{obj}}$), resulting in a total transmission $T_{total}$= 12%. Denoting $P_{laser}$ as the laser power at the fiber entrance, the total available power at the sample plane is $P_{sample} = P_{laser} \cdot T_{total}$.

However, for a fixed spot diameter at the fiber bundle, an increase in $P_{laser}$ beyond a specific threshold results in an elevated power per core, causing pulse duration broadening. For the range of laser powers used here, the pulse duration, denoted as $\tau$, can be approximated as $\tau = K \cdot P_{core} + \tau_0$, where K and $\tau_0$ represent the slope and the nominal pulse duration obtained from the linear fit in Fig. 3(b) respectively. As $P_{core}$ is the power per core, $P_{core} = P_{laser} \cdot T_{fiber}/N_{cores}$, we obtain:

$$\tau \approx \tau_0 + \mathrm{K} \cdot P_{laser} \cdot T_{fiber} \cdot \left( \frac{NA_{fiber}}{NA_{obj}} \cdot \frac{\phi_{core}}{\phi_{sample}} \right)^2 \tag{1}$$

Subsequently, designating $P_{spot}$ as the power needed to efficiently excite a target in the 2P regime (it can be the power needed to photostimulate or to image a cell for instance), the total number of targets that can be excited for a given $P_{sample}$ is $N_{spots} = \frac{P_{sample}}{P_{spot}}$, where $P_{spot}$ depends on the pulse duration. Calling $P_{spot_0}$ the power needed to excite a target when the pulse duration is $\tau_0$, we obtain $P_{spot} = P_{spot_0} \cdot \left(\frac{\tau}{\tau_0}\right)^{1/2}$ and $N_{spots} = \frac{P_{sample}}{P_{spot_0}} \left(\frac{\tau_0}{\tau}\right)^{1/2}$.

To introduce the effects of the pulse broadening, we can also define an effective power at the sample plane: $P_{eff} = P_{sample} \cdot \left(\frac{\tau_0}{\tau}\right)^{1/2}$. The total number of excitable targets is then proportional to $P_{eff}$. By combining this expression with Eq. (1), we obtain the dependence between $P_{eff}$ and $NA_{obj}$:

$$P_{eff} = P_{laser} \cdot T_{total} \left( 1 + \frac{\mathrm{K} \cdot P_{laser} \cdot T_{fiber}}{\tau_0} \cdot \left( \frac{NA_{fiber}}{NA_{obj}} \cdot \frac{\phi_{core}}{\phi_{sample}} \right)^2 \right)^{-1/2} \tag{2}$$

Biomedical Optics EXPRESS

In Fig. 6, we plot the effective power from Eq. (2) as a function of the objective NA, for different values of $P_{sample}$, obtained either by changing $P_{laser}$ (blue curves), or by optimizing the transmission of the system (such as by using a higher transmission objective, green curve). The graph assumes $\phi_{sample}$ = 15 µm and considers the parameters of the 1030 nm laser previously discussed in this manuscript (K = 43.8 fs/mW, $\tau_0$ = 160 fs). A similar graph for the 920 nm laser is given in Supp. Figure 3.

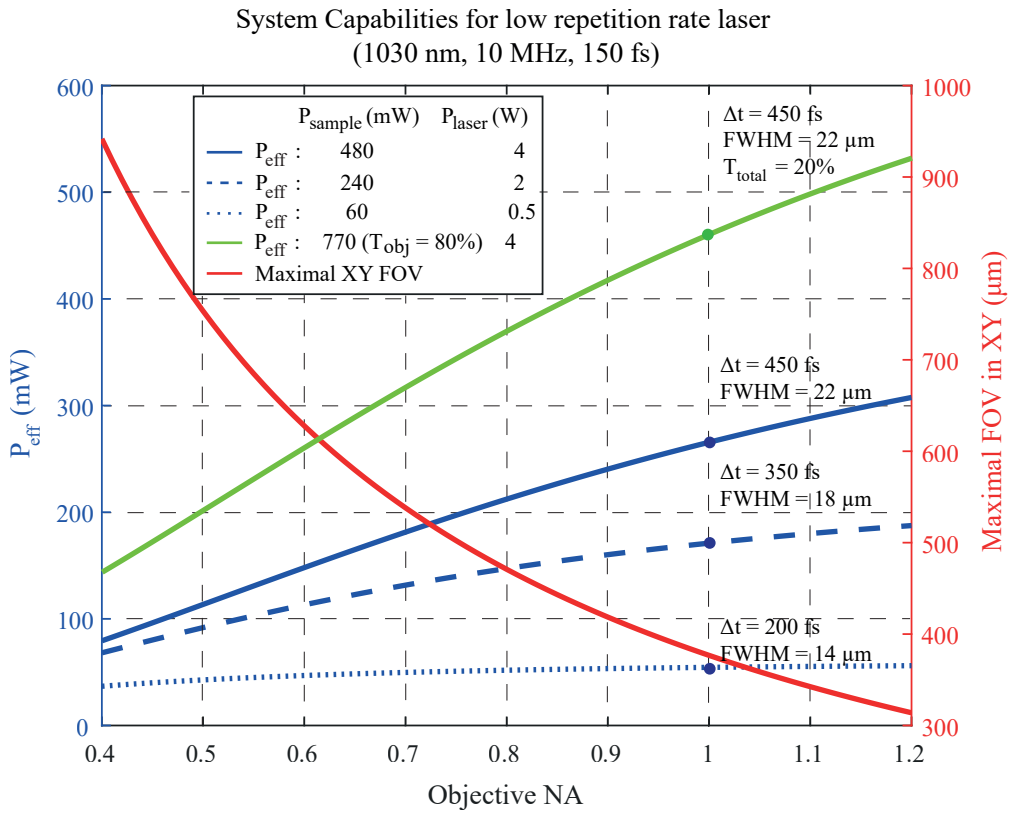


**Fig. 6. Systems capabilities and comparisons for different objective NAs.** Left vertical axis: Calculated output power from the excitation objective as a function of the effective objective NA, for the objective used in this work (with 50% transmission) and an incident wavelength of 1030 nm at a repetition rate of 10 MHz. Three different laser powers at the fiber bundle entrance are considered: 0.5 W (dashed-dotted blue curve), 2 W (dashed blue curve) and 4 W (solid blue curve), leading to different pulse broadening (200 fs, 350 fs and 450 fs respectively as indicated on top of each curve) with the corresponding measured axial resolutions. The green curve represents the maximal $P_{eff}$ that can be created considering an incident power of 4 W and an 80% transmission objective. Right vertical axis (red curve): calculated 2D FOV for different effective objective NAs using a SLM of 1272 × 1024 pixels.

Notably, the choice of the objective NA also defines the achievable FOV (see equation in Methods) (red curve, right axis). To change the objective NA does not necessarily involve replacing the objective as it is possible to underfill the objective pupil by using a different magnification between the SLM and the objective.

As illustrated, there exists a clear tradeoff between the effective power at the sample plane, which increases for higher objective NAs, and the achievable FOV's size. In practice, for a fixed $P_{laser}$ and $\phi_{sample}$, increasing $NA_{obj}$ results in a greater number of illuminated cores, lowering

Biomedical Optics EXPRESS

the power per core. This leads to a decrease of SPM, shorter laser pulse durations and more efficient 2PE. At the same time, a larger $NA_{obj}$ increases the magnification between the SLM and the objective pupil, which reduces the maximal FOV at the sample plane, for the same angles produced by the SLM.

The difference among the three blue curves demonstrates that increasing $P_{sample}$ of a given factor by turning up $P_{laser}$ only leads to an increase in $P_{eff}$ of a smaller factor (Supp. Figure 4). This is due to the fact that as the power per core increases, the 2PE becomes less efficient, especially for lower $NA_{obj}$. However, within the power range consider in our analysis, it is still beneficial to increase $P_{laser}$, up to the full 1030 nm laser power (4 W at the fiber entrance) to maximize $P_{eff}$ and, consequently, $N_{spots}$, even though it comes with a worse axial resolution. Alternatively, it is possible to increase $P_{sample}$ by minimizing the losses between the fiber and the sample. In this case, $P_{eff}$ increases by the same factor as $P_{sample}$. For example, with a 0.8 NA excitation objective with 80% transmission (which is a typical commercially available objective) and the SLM used here, one could obtain $P_{eff} = 370$ mW on a FOV of $470 \times 470$ µm$^2$ in diameter.

Another major source of power losses (50%) in our system is introduced by the PBS placed before the SLM. One possibility to compensate for this loss is to redirect the deviated beam to the SLM after rotating its polarization as show in Supp. Figure 5(a), where we could reach an almost two-fold increase of the total system transmission $T_{total}$ (from 12% to 20%). An alternative solution could use a pyramidal 4-faces mirror system [53]. Because in this configuration the two beams illuminate separately the two halves of the SLM [54], and therefore of the objective back aperture, the achievable FOV is also reduced by the half and is equal to $190 \times 190 \times 200$ µm$^3$. Larger FOVs could be reached by using a SLM with a higher pixel number.

## 4. Discussion

We have demonstrated a simple 2P microscope for multicolor axially confined 3D light patterning that uses a fiber bundle and exploits its intrinsic inter-core delay dispersion. A first advantage of using a long and flexible fiber bundle is that it makes the setup highly modular. It could for instance allow different optical setups to be coupled to the same laser sources, just by displacing the distal end of the fiber, or it could ease the integration of a photostimulation branch to an already existing imaging only microscope.

Previous approaches for 2D or 3D generation of axially confined spots have used one or two SLMs for spot shaping and beam multiplexing and a diffraction grating for temporal focusing [25–28,30–32]. Here we have demonstrated that, the diffraction grating can be replaced with similar light losses (both cases corresponding to 20-40% light loss), by a ~2-m fiber bundle. One of the primary advantages of this configuration lies in simplifying the previously proposed multiplexed temporally focused light shaping (MTF-LS [28]) configurations for the generation of three-dimensional illumination patterns. Specifically, the use of a fiber bundle, replaces the first SLM and the diffraction grating used in MTF-CGH so that one only needs the SLM for 3D light multiplexing [28]. Notably, this also preserves the flexibility to change the size (even if not the shape) of the generated spot, a flexibility that would be lost when using MTF-CGH with a fixed phase mask [8]. Typical photostimulation and neuronal imaging experiments commonly use a round-shaped spot, which aligns well the capabilities of this system.

Our configuration has also advantages with respect to the 3D-SHOT [30] configuration, which reaches three-dimensional light generation by using a single SLM but is tied to the generation of a fixed spot size, as defined by the laser's expansion. Moreover, the most recent version of 3D-SHOT [31] requires the addition of a rotating diffuser to expand the illumination to the size of the SLM, which increases the complexity of the system.

The spots generated through the fiber bundle at the sample plane present some level of inhomogeneity (see Fig. 3). This could be due to the differences in group velocity dispersion among different cores, as was experimentally demonstrated, especially for high core density

Biomedical Optics EXPRESS

fibers in Ref. [55]. Nonetheless, the same type of fiber bundles were already used both for imaging [43,56] and for photostimulation [43] of neurons in freely moving mice. Additionally, spots with inherent inhomogeneities, such as those generated by CGH that present speckles, have been employed for both 2P photostimulation and voltage imaging [35] of neuronal somas. We therefore do not expect the inhomogeneity shown here to significantly affect the imaging and/or photostimulation of somas. However, it could pose higher challenges when trying to image, with camera detection, smaller compartments of a neuron, such as dendrites or axons. In such a situation, the core-to-core inhomogeneities could be mitigated by introducing, for example, a rapid vibration based on a resonant cantilever at the output of the fiber [57,58]. This strategy would homogenize more the generated spots, at the cost of adding complexity to the optical system.

Apart from the advantage of making the system more compact and straightforward the major benefit of this configuration is that it allows for tuning the excitation wavelength or coupling multiple colors simultaneously without modifications to the optical system [41,42]. The use of a grating, in fact, requires adjusting the angle of incidence or exit for each wavelength, and for multicolor excitation, it would necessitate the use of two gratings and therefore two distinct optical paths and multiplexing SLMs. On the contrary, in our configuration, beams of different colors can be coupled into the same fiber bundle without being deflected, thus enabling using a single multiplexing SLM without beam path readjustment.

We have shown that, multicolor excitation of even the same targets can only be done accurately with an appropriate phase mask for each wavelength. This can only be achieved by sequential applying the corresponding phase masks, with a minimum temporal interval that is dictated by the SLM's refresh time, i.e. 3-16 ms with standard SLMs (refresh rates of 300-60 Hz) [11]. This is not truly a limitation for all experimental configurations in which the temporal dynamics of the phenomenon under study is longer than the refresh time. This is the case e.g. when scanless photostimulation is combined with scanless $Ca^{2+}$ imaging given the long (~80-200 ms) decay time of commonly used calcium indicators [59]. In this case, as the refresh time of the SLM is faster than the decay time of the indicators, one can sequentially switch between the photostimulation and imaging to record the effects of the photostimulation. Similarly, for experiments designed to analyze the impact on a defined behavior of an alternating sequence of activations and inhibitions, the refresh rate of the SLM should not pose a limitation.

Truly simultaneous two colors projection could otherwise be achieved by adopting the configuration reported in Supp. Figure 5, integrating the variant schematized in Supp. Figure 5(b) to control one color at each side of the SLM.

While the solution presented in this work offers many advantages compared to traditional systems, it also has its limitations in terms of maximum power, which is constrained by SPM effects [49,52]. The resulting pulse broadening has a detrimental effect on signal loss and axial resolution. Considering that SPM depends on the peak power [52], these effects are particularly significant for low repetition rate, short pulse lasers, as the 1030 nm laser used here. We have observed that for a laser with high repetition rate of 80 MHz and 920 nm excitation wavelength, it is possible to couple the total laser output power (4W) through the fiber and keep a pulse duration < 200 fs, without significant losses in the 2PE or the axial resolution. For low repetition rate lasers with comparably short initial pulses (~150 fs), the broadening effects are more pronounced, resulting in a pulse of ~400 fs for the highest powers used here. However, such a pulse duration remains comparable to the one of higher power laser systems used in conventional holographic optogenetics (10-50 W, 500 kHz-10 MHz, 300-400 fs) [11,60,61] and will thus be compatible with photostimulation. At the same time, it is possible that, for lasers with longer initial pulse durations (400 fs), the pulse broadening effect as a result of SPM, might not be as significant as in the case of shorter pulses (100-150 fs), even for the same peak power. It was indeed shown in Ref [62]· that a pulse with larger initial spectral bandwidth (shorter initial pulse

Biomedical Optics EXPRESS

duration) is more distorted and harder to temporally recompress after propagation through a fiber. This might open the way to the use of our setup to even lower repetition rate lasers with longer initial pulses. A complete characterization of SPM with different spectral bandwidths and repetition rates will allow more certain conclusions to be drawn.

To prove the capabilities of our system, we have estimated the total number of cells that we could target for photostimulation of previously reported opsins (ChroMe [31] and ChRmine [11], WicHR [63] and BIPOLE [39]); for scanless voltage imaging using the indicator JEDI-2P [35]; for scanless calcium imaging using GCaMP6 [33,34]. To do that, we have compared the $P_{eff}$ given in Fig. 6 and Supp. Figure 3, for an objective with NA = 1 and $T_{obj} = 80\%$, with the power per cell used in previous works. The detailed calculation of the maximal numbers of cells that can be targeted in different situations is provided in Supp. Table 1. In the case of photostimulation and scanless voltage imaging, by using the 1030 nm laser at 10 MHz, our system could already efficiently excite ~ 10 to 30 cells. For scanless calcium imaging, by using the 920 nm laser at 80 MHz, similar calculations show that we could target several tens, up to ~ 140 cells.

These numbers of achievable targets are compatible with a wide range of applications. They can be applied, e.g., to study how the activation of a portion or the entirety of a specific cell assembly, or even just a single hub neuron [15], can impact the circuit dynamics or to perform high-throughput intra and inter-layer connectivity mapping [16–19]. For applications where, higher total power or a greater number of achievable targets are required [11], it becomes imperative to conduct a thorough assessment of signal losses, axial resolution, and attainable output power for evaluating the benefit of using this approach compared to more traditional configurations.

## 5. Conclusions

In this study, we developed and characterized a novel fiber-based optical configuration to generate multiple axially confined illumination spots within a 2D and 3D volume using the intrinsic inter-core delay dispersion of the fiber bundles.

This configuration has two main advantages with respect to conventional optical system for multi temporal focusing light shaping, which is its simplicity and capability for multicolor excitation using a single beam path.

Despite the power per core limitation caused by SPM, we showed that the system should be already compatible with the photostimulation of few tens of cells (< 30) on a lateral FOV of $470 \times 470\ \mu m^2$ by using commercially available objectives and SLMs.

We believe that the current system will be a suitable and simple alternative in all the situations in which very large number of photostimulated cells are not needed, or in experiments requiring to project extended 2PE spots with two different colors.

**Funding.** Fondation Bettencourt Schueller (Prix Coups d'élan pour la recherche française); AXA Research Fund; Agence Nationale de la Recherche (ANR-19-CE19-0001-01, 2MEnHoloMD, ANR-23-ERCS-0009, 2P-COMFIB); European Research Council (Grant HOLOVIS ERC-2019-AdG; Award no. 885090); HORIZON EUROPE European Research Council (DEEPER, 101016787); National Institutes of Health (Brain initiative Grant 1RF1NS128772-01).

**Disclosures.** The authors declare that there are no conflicts of interest related to this article.

**Data availability.** Data underlying the results presented in this paper are not publicly available at this time but may be obtained from the authors upon reasonable request.

**Supplemental document.** See Supplement 1 for supporting content.

## References

1. E. S. Boyden, F. Zhang, K Bamberg, *et al.*, "Millisecond-timescale, genetically targeted optical control of neural activity," Nat. Neurosci. **8**(9), 1263–1268 (2005).
2. L. Fenno, O. Yizhar, and K Deisseroth, "The development and application of optogenetics," Annu. Rev. Neurosci. **34**(1), 389–412 (2011).
3. K Deisseroth, "Optogenetics: 10 years of microbial opsins in neuroscience," Nat. Neurosci. **18**(9), 1213–1225 (2015).

Biomedical Optics EXPRESS


4. V. Emiliani, Emilia Entcheva, Rainer Hedrich, *et al.*, "Optogenetics for light control of biological systems," Nat. Rev. Methods Primers **2**(1), 55 (2022).
5. K. Svoboda and R Yasuda, "Principles of Two-Photon Excitation Microscopy and Its Applications to Neuroscience," Neuron **50**(6), 823–839 (2006).
6. F. Helmchen and W Denk, "Deep tissue two-photon microscopy," Nat. Methods **2**(12), 932–940 (2005).
7. R. Conti, O. Assayag, V de Sars, *et al.*, "Computer generated holography with intensity-graded patterns," Front. Cell. Neurosci. **10**, 236 (2016).
8. A. Bañas and J Glückstad, "Holo-GPC: Holographic Generalized Phase Contrast," Opt. Commun. **392**, 190–195 (2017).
9. H. Adesnik and L Abdeladim, "Probing neural codes with two-photon holographic optogenetics," Nat. Neurosci. **24**(10), 1356–1366 (2021).
10. I. W. Chen, E. Papagiakoumou, and V. Emiliani, "Towards circuit optogenetics," Curr. Opin. Neurobiol. **50**, 179–189 (2018).
11. J. H. Marshel, Y. S. Kim, T. A. Machado, *et al.*, "Cortical layer-specific critical dynamics triggering perception," Science **365**(6453), 1 (2019).
12. Z. Zhang, L. E. Russell, M Packer, *et al.*, "Closed-loop all-optical interrogation of neural circuits in vivo," Nat. Methods **15**(12), 1037–1040 (2018).
13. J. V. Gill, Gilad M. Lerman, Hetince Zhao, *et al.*, "Precise Holographic Manipulation of Olfactory Circuits Reveals Coding Features Determining Perceptual Detection," Neuron **108**(2), 382–393.e5 (2020).
14. L. Carrillo-Reid, S. Han, R Yang, *et al.*, "Controlling Visually Guided Behavior by Holographic Recalling of Cortical Ensembles," Cell **178**(2), 447–457.e5 (2019).
15. Y. Bollmann, Laura Modol, Thomas Tressard, *et al.*, "Prominent in vivo influence of single interneurons in the developing barrel cortex," Nat. Neurosci. **26**(9), 1555–1565 (2023).
16. I.-W. Chen, C.Y. Chan, P. Navarro, *et al.*, "High-throughput in vivo synaptic connectivity mapping of neuronal micro-circuits using two-photon holographic optogenetics and compressive sensing," bioRxiv, bioRxiv:2023.09.11.557026 (2023).
17. Y. Printz, P. Patil, M. Mahn, *et al.*, "Determinants of functional synaptic connectivity among amygdala-projecting prefrontal cortical neurons in male mice," Nat. Commun. **14**(1), 1 (2023).
18. C. McRaven, D. Tanese, L. Zhang, *et al.*, "High-throughput cellular-resolution synaptic connectivity mapping in vivo with concurrent two-photon optogenetics and volumetric Ca 2 + imaging," bioRxiv, bioRxiv:2020.02.21.959650 (2020).
19. T. A. Hage, A. Bosma-MoodyChristopher, A. Baker, *et al.*, "Synaptic connectivity to L2/3 of primary visual cortex measured by two-photon optogenetic stimulation," Elife **11**, 1–46 (2022).
20. J. P. Rickgauer and D. W Tank, "Two-photon excitation of channelrhodopsin-2 at saturation," Proc. Natl. Acad. Sci. U. S. A. **106**(35), 15025–15030 (2009).
21. E. Ronzitti, Cathie Ventalon, Marco Canepari, *et al.*, "Recent advances in patterned photostimulation for optogenetics," J. Opt. **19**(11), 113001 (2017).
22. G. Zhu, J. van Howe, C Durst, *et al.*, "Simultaneous spatial and temporal focusing of femtosecond pulses," Opt. Express **13**(6), 2153–2159 (2005).
23. E. Tal, D. Oron, and Y Silberberg, "Improved depth resolution in video-rate line-scanning multiphoton microscopy using temporal focusing," Opt. Lett. **30**(13), 1686 (2005).
24. D. Oron, E. Tal, and Y. Silberberg, "Scanningless depth-resolved microscopy," Opt. Express **13**(5), 1468 (2005).
25. E. Papagiakoumou, Francesca Anselmi, Aurélien Bègue, *et al.*, "Scanless two-photon excitation of channelrhodopsin-2," Nat. Methods **7**(10), 848–854 (2010).
26. E. Papagiakoumou, V. de Sars, V Oron, *et al.*, "Patterned two-photon illumination by spatiotemporal shaping of ultrashort pulses," Opt. Express **16**(26), 22039 (2008).
27. O. Hernandez, Eirini Papagiakoumou, Dimitrii Tanese, *et al.*, "Three-dimensional spatiotemporal focusing of holographic patterns," Nat. Commun. **7**(1), 11928 (2016).
28. N. Accanto, Clément Molinier, Dimitrii Tanese, *et al.*, "Multiplexed temporally focused light shaping for high-resolution multi-cell targeting," Optica **5**(11), 1478 (2018).
29. E. Papagiakoumou, E. Ronzitti, and V Emiliani, "Scanless two-photon excitation with temporal focusing," Nat. Methods **17**(6), 571–581 (2020).
30. N. C. Pégard, Alan R. Mardinly, Ian Antón Oldenburg, *et al.*, "Three-dimensional scanless holographic optogenetics with temporal focusing (3D-SHOT)," Nat. Commun. **8**(1), 1228 (2017).
31. A. R. Mardinly, Ian Antón Oldenburg, Nicolas C. Pégard, *et al.*, "Precise multimodal optical control of neural ensemble activity," Nat. Neurosci. **21**(6), 881–893 (2018).
32. G. Faini, D. Tanese, C. Molinier, *et al.*, "Ultrafast light targeting for high-throughput precise control of neuronal networks," Nat. Commun. **14**(1), 1888 (2023).
33. C. Moretti, A. Antonini, T Bovetti, *et al.*, "Scanless functional imaging of hippocampal networks using patterned two-photon illumination through GRIN lenses," Biomed. Opt. Express **7**(10), 3958 (2016).
34. S. Bovetti, Claudio Moretti, Stefano Zucca, *et al.*, "Simultaneous high-speed imaging and optogenetic inhibition in the intact mouse brain," Sci. Rep. **7**(1), 40041 (2017).
35. R. R. Sims, et al. Scanless two-photon voltage imaging. Res. Sq. Under revi, (2023).

Biomedical Optics EXPRESS


36. R. Prevedel, Aart J Verhoef, Alejandro J Pernía-Andrade, *et al.*, "Fast volumetric calcium imaging across multiple cortical layers using sculpted light," Nat. Methods **13**(12), 1021–1028 (2016).
37. A. Forli, Dania Vecchia, Noemi Binini, *et al.*, "Two-Photon Bidirectional Control and Imaging of Neuronal Excitability with High Spatial Resolution In Vivo," Cell Rep. **22**(11), 3087–3098 (2018).
38. Y. Shymkiv and R Yuste, "Aberration-free holographic microscope for simultaneous imaging and stimulation of neuronal populations," Opt. Express **31**(20), 33461 (2023).
39. J. Vierock, S. Rodriguez-Rozada, A. Dieter, *et al.*, "BiPOLES is an optogenetic tool developed for bidirectional dual-color control of neurons," Nat. Commun. **12**(1), 4527 (2021).
40. K. Erbguth, M. Prigge, A Schneider, *et al.*, "Bimodal Activation of Different Neuron Classes with the Spectrally Red-Shifted Channelrhodopsin Chimera C1V1 in Caenorhabditis elegans," PLoS One **7**(10), e46827 (2012).
41. C.-H. Lien, G. Abrigo, F.-C Chen, *et al.*, "Two-color temporal focusing multiphoton excitation imaging with tunable-wavelength excitation," J. Biomed. Opt. **22**(2), 026008 (2017).
42. Y.-M. M. Cheng, C.-H. H. Lien, F.-C. C Ke, *et al.*, "An excitation wavelength switching to enhance dual-color wide-field temporal-focusing multiphoton excitation fluorescence imaging," J. Phys. D: Appl. Phys. **53**(23), 235401 (2020).
43. N. Accanto, François G.C. Blot, Antonio Lorca-Cámara, *et al.*, "A flexible two-photon fiberscope for fast activity imaging and precise optogenetic photostimulation of neurons in freely moving mice," Neuron **111**(2), 176–189.e6 (2023).
44. L. Golan, I. Reutsky, S Farah, *et al.*, "Design and characteristics of holographic neural photo-stimulation systems," J. Neural Eng. **6**(6), 066004 (2009).
45. R. W. Gerchberg and S. W. O, "A Practical Algorithm for the Determination of Phase from Image and Diffraction Plane Pictures," Optik **35**, 237–246 (1971).
46. J. Lee and D Kim, "Large-scale 3D fast Fourier transform computation on a GPU," ETRI J. **45**, 1035–1045 (2023).
47. S. Chen and X. Li, "A hybrid GPU/CPU FFT library for large FFT problems," in *2013 IEEE 32nd International Performance Computing and Communications Conference, IPCCC 2013* 1–10 (2013).
48. E. R. Andresen, Siddharth Sivankutty, Géraud Bouwmans, *et al.*, "Measurement and compensation of residual group delay in a multi-core fiber for lensless endoscopy," J. Opt. Soc. Am. B **32**(6), 1221 (2015).
49. M. T. Myaing, J. Urayama, T. B Braun, *et al.*, "Nonlinear propagation of negatively chirped pulses: maximizing the intensity at the output of a fiber probe," Opt. Express **7**(5), 210–214 (2000).
50. H. Bao, J. Allen, M Pattie, *et al.*, "Fast handheld two-photon fluorescence microendoscope with a 475 µm × 475 µm field of view for in vivo imaging," Opt. Lett. **33**(12), 1333 (2008).
51. M. Oberthaler and R. A Höpfel, "Special narrowing of ultrashort laser pulses by self-phase modulation in optical fibers," Appl. Phys. Lett. **63**(8), 1017–1019 (1993).
52. F. Helmchen, D. W. Tank, and W Denk, "Enhanced two-photon excitation through optical fiber by single-mode propagation in a large core," Appl. Opt. **41**(15), 2930 (2002).
53. M. P. Backlund, Matthew D. Lew, Adam S. Backer, *et al.*, "Simultaneous, accurate measurement of the 3D position and orientation of single molecules," Proc. Natl. Acad. Sci. U. S. A. **109**(47), 19087–19092 (2012).
54. J. Ren and K. Y Han, "2.5D microscopy with polarization independent SLM for enhanced detection efficiency and aberration correction," Opt. Express **29**(17), 27530 (2021).
55. A. Garofalakis, Sergei G. Kruglik, Tigran Mansuryan, *et al.*, "Characterization of a multicore fiber image guide for nonlinear endoscopic imaging using two-photon fluorescence and second-harmonic generation," J. Biomed. Opt. **24**(10), 1 (2019).
56. B. N. Ozbay, Gregory L. Futia, Ming Ma, *et al.*, "Three dimensional two-photon brain imaging in freely moving mice using a miniature fiber coupled microscope with active axial-scanning," Sci. Rep. **8**(1), 8108 (2018).
57. M. T. Myaing, D. J. MacDonald, and X Li, "Fiber-optic scanning two-photon fluorescence endoscope," Opt. Lett. **31**(8), 1076 (2006).
58. A. Li, Honghua Guan, Hyeon-Cheol Park, *et al.*, "Twist-free ultralight two-photon fiberscope enabling neuroimaging on freely rotating/walking mice," Optica **8**(6), 870 (2021).
59. Y. Zhang, Márton Rózsa, Yajie Liang, *et al.*, "Fast and sensitive GCaMP calcium indicators for imaging neural populations," Nature **615**(7954), 884–891 (2023).
60. S. Sridharan, Marta A. Gajowa, Mora B. Ogando, *et al.*, "High-performance microbial opsins for spatially and temporally precise perturbations of large neuronal networks," Neuron **110**(7), 1139–1155.e6 (2022).
61. A. M. Packer, L. E. Russell, M Dalgleish, *et al.*, "Simultaneous all-optical manipulation and recording of neural circuit activity with cellular resolution in vivo," Nat. Methods **12**(2), 140–146 (2015).
62. M. Kalashyan, Claire Lefort, Lluís Martínez-León, *et al.*, "Ultrashort pulse fiber delivery with optimized dispersion control by reflection grisms at 800 nm," Opt. Express **20**(23), 25624 (2012).
63. J. Vierock, E. Peter, C. Grimm, *et al.*, "WiChR, a highly potassium-selective channelrhodopsin for low-light one- and two-photon inhibition of excitable cells," Sci. Adv. **8**(49), 1–18 (2022).